

# Deep Learning for Simultaneous Inference of Hydraulic and Transport Properties

Zitong Zhou<sup>1</sup>, Nicholas Zabaras<sup>2</sup>, and Daniel M. Tartakovsky<sup>1</sup>

<sup>1</sup>Department of Energy Resources Engineering, Stanford University, Stanford, CA 94305, USA

<sup>2</sup>Scientific Computing and Artificial Intelligence (SCAI) Laboratory, University of Notre Dame, South Bend, IN 46556, USA

## Key Points:

- We present a deep-learning strategy to reconstruct conductivity and contaminant release history in three-dimensional heterogeneous aquifers.
- Conductivity parameterization with convolutional adversarial autoencoder reduces the inverse problem's dimensionality.
- Convolutional encoder-decoder acts as a surrogate of forward models; ensemble smoother approximates parameters' posterior distribution.

---

Corresponding author: Daniel M. Tartakovsky, [tartakovsky@stanford.edu](mailto:tartakovsky@stanford.edu)

Corresponding author: Nicholas Zabaras, [nzabaras@gmail.com](mailto:nzabaras@gmail.com)

## Abstract

Identifying the heterogeneous conductivity field and reconstructing the contaminant release history are key aspects of subsurface remediation. Achieving these two goals with limited and noisy hydraulic head and concentration measurements is challenging. The obstacles include solving an inverse problem for high-dimensional parameters, and the high-computational cost needed for the repeated forward modeling. We use a convolutional adversarial autoencoder (CAAE) for the parameterization of the heterogeneous non-Gaussian conductivity field with a low-dimensional latent representation. Additionally, we trained a three-dimensional dense convolutional encoder-decoder (DenseED) network to serve as the forward surrogate for the flow and transport processes. Combining the CAAE and DenseED forward surrogate models, the ensemble smoother with multiple data assimilation (ESMDA) algorithm is used to sample from the Bayesian posterior distribution of the unknown parameters, forming a CAAE-DenseED-ESMDA inversion framework. We applied this CAAE-DenseED-ESMDA inversion framework in a three-dimensional contaminant source and conductivity field identification problem. A comparison of the inversion results from CAAE-ESMDA with physical flow and transport simulator and CAAE-DenseED-ESMDA is provided, showing that accurate reconstruction results were achieved with a much higher computational efficiency.

## 1 Introduction

Design of regulatory and remedial actions for contaminated soils and aquifers rely on reconstruction of the contaminant release history. Given subsurface heterogeneity, this task is inseparable from the need to identify hydraulic and transport properties of the subsurface environment. Both tasks have to contend with sparse and noisy measurements collected many years or decades after the contamination event took place. Prior to recent breakthroughs in computer architecture and algorithmic development, this joint inversion of hydraulic and water-quality data for real-world problems was so demanding computationally as to defy a solution unless dramatic (and often unrealistic) simplifications of the problem were made. For example, past efforts to reconstruct a contaminant release history found it necessary to assume solute migration to be one- or two-dimensional and subsurface properties, such as hydraulic conductivity  $K(\mathbf{x})$ , to be known with certainty (Aral et al., 2001; Snodgrass & Kitanidis, 1997; Yeh et al., 2007, among many others). Yet, aquifers are seldom, if ever, homogeneous, with  $K(\mathbf{x})$  often varying by orders of magnitude within the same aquifer and exhibiting highly non-Gaussian, multimodal behavior (Tartakovsky & Winter, 2008; Winter et al., 2003; Yang et al., 2020). Likewise, while the assumption of two-dimensional groundwater flow is often valid, accounting for the three-dimensional nature of contaminant migration is essential to prediction accuracy.

Our effort in joint inversion of hydraulic conductivity and contaminant release history from error-prone measurements of hydraulic head and solute concentration revolves around two challenges. The first is to describe the unknown non-Gaussian heterogeneous conductivity field with an adequate prior distribution. The second is to estimate a large number of unknown parameters in the inverse problem.

To tackle the first challenge, a parameterization of the high-dimensional conductivity field with a low-dimensional latent variable is commonly used (Linde et al., 2015; H. Zhou et al., 2014). Parameterizations based on the principle component analysis (PCA) (Sarma et al., 2008; Vo & Durlofsky, 2014) perform well for Gaussian random fields, but require ad-hoc modifications for non-Gaussian fields (Liu et al., 2019). DNN-based parameterizations eliminate the need for the Gaussianity assumption (Canchumuni et al., 2019; Liu et al., 2019). Two popular methods of this class are the generative adversarial network (GAN) (I. J. Goodfellow et al., 2014) and

variational autoencoders (Kingma & Welling, 2013). Both produce a DNN that learns a two-way mapping between the conductivity field and a low-dimensional embedding. Random realizations from the latent variable distribution can be decoded to a conductivity field that is statistically similar to those drawn from the training data set. In addition to the large reduction in the number of the unknown parameters, such parameterizations make it feasible to tackle the latent variable distribution, which is typically a standard normal by construction. This simplicity, in turn, facilitates the solution of the inverse problem with ensemble methods discussed below.

The second challenge, high-dimensionality of the parameter space, manifests itself in significant computational burden of an inversion procedure. Parameter estimation, which lies at the heart of an inverse problem, is achieved by matching the noisy measurements with the prediction of a flow and solute transport model. Strategies for solving typical ill-posed inverse problems fall into two main categories, deterministic and probabilistic. Deterministic methods, such as least square regression (White, 2015) and hybrid optimization with a genetic algorithm (Ayvaz, 2016; Leichombam & Bhattacharjya, 2018), seek a “best” estimate of the unknown parameters, without quantifying the uncertainty inherent in this type of problems. Probabilistic methods, such as Markov Chain Monte Carlo or MCMC (Gelman & Lopes, 2006) and data assimilation via Kalman filters (Evensen, 1994, 2003; Xu & Gómez-Hernández, 2016, 2018) and their variants (Emerick & Reynolds, 2013; Zhang et al., 2018), overcome this shortcoming of their deterministic counterparts. Yet, the high-cost of necessary repeated forward solves undermines their utility for large, complex inverse problems, unless dedicated high-performance computing facilities are available for the task.

Two complementary strategies can be deployed to alleviate this cost. The first aims to reduce the number of forward simulations needed for an inversion algorithm to converge. The second seeks to reduce the computational cost of each forward solve. Efforts in the former direction include the design of efficient MCMC variants, such as delayed rejection adaptive Metropolis (DRAM) sampling (Haario et al., 2001, 2006) which slightly outperforms a random walk Metropolis-Hastings MCMC in terms of efficiency (Zhang et al., 2015; Z. Zhou & Tartakovsky, 2021; Xia & Zabaras, 2021). Gradient-based MCMC methods, such as hybrid Monte Carlo (HMC) sampling (Barajas-Solano et al., 2019), converge faster than these and other MCMC variants. However, computation of the gradient of a Hamiltonian dynamical system is prohibitive for high-dimensional transport problems. Learning on statistical manifolds provides another possible solution (Boso & Tartakovsky, 2020b, 2020a). Ensemble-based inversion methods are generally faster since they allow nearly perfect parallelization, because of the independence of samples in the ensemble. Variants of Kalman filters, such as iterative Ensemble Kalman filter (IEnKF), have been used for estimation of three-dimensional heterogeneous permeability fields (Chaudhuri et al., 2018). A relatively new variant of Kalman filter, ensemble smoother with multiple data assimilation (ESMDA) (Emerick & Reynolds, 2013), has gained popularity in subsurface flow history matching (Tang et al., 2021; Kim et al., 2019; Jiang & Durlafsky, 2021).

In terms of inversion complexity, we subdivide recent groundwater-related studies into three categories: estimation of hydraulic conductivity from measurements of hydraulic head and, optionally, of solute concentration (Mo et al., 2019b; Ju et al., 2018); estimation of contaminant release history from concentration measurements, for known flow and transport parameters (Z. Zhou & Tartakovsky, 2021; Zhang et al., 2015); and estimation of both contaminant release history and hydraulic conductivity from hydraulic head and solute concentration data in two- (Mo et al., 2019a; Xu & Gómez-Hernández, 2018; Kang et al., 2021) and three-dimensional (Kang et al., 2020) aquifers. We briefly discuss the latter category to highlight the novelty of our approach.

A low-dimensional representation of the random log-normal conductivity obtained via the Karhunen-Loève expansion (KLE) in (Mo et al., 2019a) loses its attractiveness if the subsurface environment is highly heterogeneous, exhibiting short correlation lengths and multimodal statistics; additionally, this study relies on a linear transport model. The deep learning-based strategies of ensemble inversion were adopted in (Xu & Gómez-Hernández, 2018; Kang et al., 2021) to estimate both a non-Gaussian conductivity field and the source of contamination, yet their reported accuracy is relatively low. In the adjacent field of petroleum engineering, CNN post-processing of PCA (CNN-PCA) parameterization and ESMDA were used to estimate both a channelized permeability and the oil/water rate (Tang et al., 2021). However, this application deals with an observable quantity (the oil/water production rate), while ours has to contend with an unobservable one (the location and strength of a contaminant release).

To address the shortcomings of the joint inversion strategies mentioned above, we use a convolutional adversarial autoencoder (CAAE) to parameterize a non-Gaussian conductivity field (Mo et al., 2019b), train a surrogate dense encoder-decoder DNN to replace the PDE-based model of subsurface flow and transport, and apply the ESMDA inversion framework to identify the spatiotemporally extended source of contamination and the latent variables representing the conductivity field. We posit that combination of these three components, which yields the method we refer to as CAAE-DenseED-ESMDA, provides a fast and robust inversion solution.

In Section 2, we formulate the problem of joint reconstruction of hydraulic conductivity field and contaminant release history from sparse and noisy measurements of hydraulic head and solute concentration. Our inversion strategy, combining CAAE parameterization of the conductivity field (Section 3.2), a convolutional DNN surrogate of the flow and transport model (Section 3.3), and the ESMDA inversion method (Section 3.1), is described in Section 3. Results of our numerical experiments are reported in Section 4; they demonstrate that our method is about 8 times faster than CAAE-ESMDA with the PDE-based flow and transport model. Main conclusions drawn from this study are summarized in Section 5. The details of the neural network architectures are given in Appendix A. The datasets and the code needed to reproduce the results can be downloaded after publication of this work from <https://github.com/zabaras/3dinversion>.

## 2 Problem Formulation

The problem formulation consists of the description of a reactive transport model (Section 2.1) and the specification of a data model (Section 2.2).

### 2.1 Contaminant Transport Model

We consider transport of a reactive solute in a three-dimensional steady-state groundwater flow field. The latter is described by:

$$\nabla \cdot (K \nabla h) = 0, \quad \mathbf{x} = (x_1, x_2, x_3)^\top \in \Omega \subset \mathbb{R}^3, \quad (1)$$

where  $K(\mathbf{x})$  is the hydraulic conductivity of the aquifer  $\Omega$ , and  $h(\mathbf{x})$  is the hydraulic head. This PDE is subject to appropriate boundary conditions on the simulation domain boundary  $\partial\Omega$ . After the flow equation is solved, the average pore velocity  $\mathbf{u}(\mathbf{x}) = (u_1, u_2, u_3)^\top$  is computed from Darcy's law,

$$\mathbf{u} = -\frac{K}{\theta} \nabla h, \quad (2)$$

where  $\theta(\mathbf{x})$  is the aquifer's porosity.



Starting at some unknown time  $t_0$ , a contaminant with volumetric concentration  $c_s$  enters the aquifer through either point-wise or spatially distributed sources  $\Omega_s \subset \Omega$ . The contaminant is released for an unknown duration  $T$  with unknown intensity  $q_s(\mathbf{x}, t)$  (volumetric flow rate per unit source volume), such that  $q_s(\mathbf{x}, t) \neq 0$  for  $t_0 \leq t \leq t_0 + T$ . The contaminant is advected by the flow, while undergoing hydrodynamic dispersion and sorption to the solid matrix with rate  $R_n$ . Without loss of generality, the spatiotemporal evolution of the contaminant's volumetric concentration  $c(\mathbf{x}, t)$  is described by an advection-dispersion-reaction equation:

$$\frac{\partial \theta c}{\partial t} = \nabla \cdot (\theta \mathbf{D} \nabla c) - \nabla \cdot (\theta \mathbf{u} c) - R_n(c) + q_s c_s, \quad \mathbf{x} \in \Omega, \quad t > t_0, \quad (3)$$

where the dispersion coefficient  $\mathbf{D}$  is a semi-positive second-rank tensor. If the coordinate system is aligned with the mean flow direction, such that  $\mathbf{u} = (u \equiv |\mathbf{u}|, 0, 0)^\top$ , then the components of this tensor are:

$$D_{11} = \theta D_m + \alpha_L u, \quad D_{22} = \theta D_m + \alpha_T u, \quad D_{33} = \theta D_m + \alpha_C u, \quad D_{ij} = \theta D_m \text{ for } i \neq j, \quad (4)$$

where  $D_m$  is the coefficient of molecular diffusion for the contaminant in free water;  $\alpha_L$  is the longitudinal dispersivity; and  $\alpha_T$  and  $\alpha_C$  are transverse dispersivities in the  $x_2$  and  $x_3$  directions, respectively.

The chemical reactions considered represent sorption of the dissolved contaminant onto the solid surface of the porous media. Thus, the reaction terms  $R_n(c)$  take the form:

$$R_n(c) = -\rho_b \frac{\partial \tilde{c}}{\partial t}, \quad (5)$$

where  $\rho_b$  is the bulk density and  $\tilde{c}$  is the concentration sorbed.

We assume the system to be in local chemical equilibrium, i.e., sorption to be much faster than advection and dispersion. We also assume that sorption does not affect the porosity  $\theta$ , which remains constant throughout the simulations. With these assumptions, (3) reduces to:

$$R\theta \frac{\partial c}{\partial t} = \nabla \cdot (\theta \mathbf{D} \nabla c) - \nabla \cdot (\theta \mathbf{u} c) + q_s c_s, \quad (6)$$

wherein  $R(c)$  is the dimensionless retardation factor defined as:

$$R = 1 + \frac{\rho_b}{\theta} \frac{\partial \tilde{c}}{\partial c}. \quad (7)$$

A sorption isotherm defines the relationship between the sorbed concentration,  $\tilde{c}$ , and the dissolved concentration,  $c$ . Among the popular isotherms—linear, Langmuir, and Freundlich—we adopt the latter, for the sake of concreteness. According to the Freundlich isotherm,

$$\tilde{c} = K_f c^a, \quad (8)$$

where  $K_f$  is the Freundlich constant,  $(L^3 M^{-1})^a$ ; and  $a$  is the Freundlich exponent. The units of all relevant transport quantities are summarized in Table 1.

**Table 1.** *Quantities in the transport model (6) and their units.*

Term	Physical quantity	Units
$c$	dissolved concentration	$\text{ML}^{-3}$
$\theta$	porosity of the subsurface medium	-
$x_i$	the distance along the respective Cartesian coordinate axis	L
$D_{ij}$	hydrodynamic dispersion coefficient tensor	$\text{L}^2\text{T}^{-1}$
$u_i$	pore water velocity	$\text{LT}^{-1}$
$q_s$	volumetric flow rate per volume, sources (+) and sinks (-)	$\text{T}^{-1}$
$c_s$	concentration of source or sink flux	$\text{ML}^{-3}$
$R_n$	chemical reaction term	$\text{ML}^{-3}\text{T}^{-1}$
$\rho_b$	bulk density of the medium	$\text{ML}^{-3}$
$\bar{c}$	concentration sorbed	$\text{ML}^{-3}$
$K_f$	Freundlich constant	$(\text{L}^3\text{M}^{-1})^a$
$a$	Freundlich exponent	-

## 2.2 Parameters of Interest

Our goal is to identify the conductivity field  $K(\mathbf{x})$  and the contaminant source  $q_s c_s(\mathbf{x}, t)$ , given the flow and transport models, (1)–(8), and measurements of contaminant concentration and hydraulic head. Other parameters in the transport model, such as porosity, reaction term coefficients, etc., are assumed to be known. Identification of the source term  $q_s c_s$  is tantamount to finding the location(s),  $\mathbf{S}_1$ , and strength,  $\mathbf{S}_s \in \mathbb{R}^{N_{\text{re}}}$ , of the contaminant source; with the elements  $S_{sj}$  ( $j = 1, \dots, N_{\text{re}}$ ) of the vector  $\mathbf{S}_s$  denoting the release strength at the  $j$ -th time interval.

Measurements of hydraulic head,  $\bar{h}_m = \bar{h}(\mathbf{x}_m)$ , and solute concentration,  $\bar{c}_{mi} = \bar{c}(\mathbf{x}_m, t_i)$ , are collected at locations  $\{\mathbf{x}_m\}_{m=1}^M$  at times  $\{t_i\}_{i=1}^I$ . In lieu of field observations, we generate these data by corrupting the solution of (1)–(8) obtained for the reference parameter values by random measurement errors  $\epsilon_{mi}^c$  and  $\epsilon_m^h$ , such that:

$$\bar{c}_{m,i} = c(\mathbf{x}_m, t_i) + \epsilon_{mi}^c, \quad \bar{h}_m = h(\mathbf{x}_m) + \epsilon_m^h; \quad m = 1, \dots, M, \quad i = 1, \dots, I, \quad (9)$$

where  $c(\mathbf{x}_m, t_i)$  and  $h(\mathbf{x}_m)$  are the model predictions. The zero-mean Gaussian random variables  $\epsilon_{mi}^c$  have covariance  $\mathbb{E}[\epsilon_{mi}^c \epsilon_{nj}^c] = \delta_{ij} R_{mn}^c$ , where  $\mathbb{E}[\cdot]$  denotes the ensemble mean;  $\delta_{ij}$  is the Kronecker delta function; and  $R_{mn}^c$  with  $m, n \in [1, M]$  are components of the  $M \times M$  spatial covariance matrix  $\mathbf{R}^c$  of measurements errors. To be specific, we set  $\mathbf{R}^c = \sigma_c^2 \mathbf{I}$ , where  $\sigma_c$  is the standard deviation of the measurement errors, and  $\mathbf{I}$  is the  $(M \times M)$  identity matrix. The hydraulic head measurement errors  $\epsilon_m^h$  are zero-mean Gaussian random variables with covariance  $\mathbb{E}[\epsilon_m^h \epsilon_n^h] = R_{mn}^h$  with  $m, n \in [1, M]$ . We set  $\mathbf{R}^h = \sigma_h^2 \mathbf{I}$ , where  $\sigma_h$  is the standard deviation of the measurement errors.

The error model in (9) assumes the flow and transport models (1)–(8) to be exact and the measurements errors to be unbiased and uncorrelated in time but not in space. The groundwater flow equation is solved with MODFLOW (Harbaugh, 2005), and the solute transport equation with MT3DMS (Zheng & Wang, 1999; Bedekar et al., 2016). We use Flopy (Bakker et al., 2016), a Python implementation of these two packages.

## 3 Methodology

Below we describe the three elements of our inversion framework: ensemble smoother with multiple data assimilation (ESMDA), convolutional adversarial autoencoder (CAAE) parameterization of the conductivity field, and a Dense encoder-decoder (DenseED) neural network surrogate of the forward model.

### 3.1 Ensemble Smoother with Multiple Data Assimilation (ESMDA)

Upon a spatiotemporal discretization, the uncertain (random) input parameters in (1)–(4) are rearranged into a vector  $\mathbf{m}$  of length  $N_m$ ; these inputs include the discretized source term ( $\mathbf{S}_1, \mathbf{S}_s$ ) and hydraulic conductivity  $K(\mathbf{x})$  in all discretized cells (in the applications in this study,  $K(\mathbf{x})$  is parameterized with a low dimensional variable, illustrated in detail in Section 3.2). Similarly, we arrange the random measurements  $\bar{c}_{m,i}$  and  $\bar{h}_m$  into a vector  $\mathbf{d}$  of length  $N_d = M(I + 1)$ , and the random measurement noise  $\epsilon_{mi}^c$  and  $\epsilon_m^h$  into a vector  $\boldsymbol{\varepsilon}$  of the same length. Then, the error model (9) takes the vector form,

$$\mathbf{d} = \mathbf{g}(\mathbf{m}) + \boldsymbol{\varepsilon}, \quad (10)$$

where  $\mathbf{g}(\cdot)$  is the vector, of length  $N_d$ , of the correspondingly arranged stochastic model predictions  $c(\mathbf{x}_m, t_i)$  and  $h(\mathbf{x}_m)$  predicated on the model inputs  $\mathbf{m}$ . Let  $\pi(\mathbf{m})$  denote a prior PDF of the inputs  $\mathbf{m}$ , which encapsulates the knowledge about the aquifer's properties and contaminant source before any measurements are assimilated. Our goal is to improve this prior by assimilating the measurements  $\mathbf{d}$ , i.e., to compute the posterior PDF of the model parameters,  $\pi(\mathbf{m}|\mathbf{d})$ . This task is accomplished via Bayes' rule,

$$\pi(\mathbf{m}|\mathbf{d}) = \frac{\pi(\mathbf{m})\pi(\mathbf{d}|\mathbf{m})}{\pi(\mathbf{d})}, \quad \pi(\mathbf{d}) = \int \pi(\mathbf{m})\pi(\mathbf{d}|\mathbf{m})d\mathbf{m}, \quad (11)$$

where  $\pi(\mathbf{d}|\mathbf{m})$  is the likelihood function; and  $\pi(\mathbf{d})$ , is the “evidence” that serves as a normalizing constant so that  $\pi(\mathbf{m})\pi(\mathbf{d}|\mathbf{m})$  integrates to 1.

To compute (11), we use ESMDA (Emerick & Reynolds, 2013), which is an ensemble updating method similar to ensemble smoother (ES) (Van Leeuwen & Evensen, 1996) or ensemble Kalman filter (EnKF) (Evensen, 1994, 2003). To place ESMDA in the proper perspective, we briefly describe ES. The method is initiated by drawing  $N_e$  samples  $\mathbf{M}^f = \{\mathbf{m}_1^f, \dots, \mathbf{m}_{N_e}^f\}$  from the prior PDF  $\pi(\mathbf{m})$ . These data are then updated as:

$$\mathbf{m}_j^a = \mathbf{m}_j^f + \mathbf{C}_{\text{MD}}^f (\mathbf{C}_{\text{DD}}^f + \mathbf{C}_{\text{D}})^{-1} [\mathbf{d}_{uc,j} - g(\mathbf{m}_j^f)], \quad j = 1, \dots, N_e, \quad (12)$$

forming  $\mathbf{M}^a = [\mathbf{m}_1^a, \dots, \mathbf{m}_{N_e}^a]$ , the updated ensemble conditioned on the measurements  $\mathbf{d}$ . Here,  $\mathbf{C}_{\text{D}} \in \mathbb{R}^{N_d \times N_d}$  is the covariance matrix of the measurement errors  $\boldsymbol{\varepsilon}$ ; we define an ensemble of perturbed measurements:  $\{\mathbf{d}_{uc,j}\}_{j=1}^{N_e}$ , which are obtained by sampling from the Gaussian distribution:  $\mathbf{d}_{uc,j} \sim \mathcal{N}(\mathbf{d}, \mathbf{C}_{\text{D}})$ ;  $\mathbf{C}_{\text{DD}}^f \in \mathbb{R}^{N_d \times N_d}$  is the auto-covariance matrix of the model predictions  $\mathbf{D}^f = \mathbf{D}^f = [g(\mathbf{m}_1^f), \dots, g(\mathbf{m}_{N_e}^f)]$ ; and  $\mathbf{C}_{\text{MD}}^f \in \mathbb{R}^{N_m \times N_d}$  is the cross-covariance matrix between  $\mathbf{M}^f$  and  $\mathbf{D}^f$ . During the update, all the data  $\mathbf{d}$  are used once, simultaneously. This global update may cause an unacceptably large mismatch between the model response and the measurements, which precipitated the development of an iterative ES with smaller-scale updates.

While ES performs a single large Gauss-Newton correction to the ensemble  $\mathbf{M}^f$ , ESMDA makes a smaller correction during each update and deploys the inflated covariance matrix  $\mathbf{C}_{\text{D}}$  to damp the changes in the ensemble at early iterations (Gao & Reynolds, 2004; Wu et al., 1999). (In the linear Gaussian case, ESMDA and ES yield identical results.) We use the following algorithm to implement ESMDA.

- Set the number of data assimilation iterations,  $N_a$ , and the corresponding inflation coefficients  $\alpha_i$   $i = 1, \dots, N_a$ . Requiring  $\sum_{i=1}^{N_a} \alpha_i = 1$  guarantees consistency with ES in the linear Gaussian case. Generate the initial ensemble  $\mathbf{m}_j^1$  ( $j = 1, \dots, N_e$ ) from the prior PDF  $\pi(\mathbf{m})$ .
- Repeat the following steps for  $i = 1, \dots, N_a$ :
  1. Run the forward simulation for each member  $\mathbf{m}_j^i$  ( $j = 1, \dots, N_e$ ) from the parameter ensemble  $\mathbf{M}^f$  to obtain the corresponding model predictions (and in the synthetic case, observations)  $g(\mathbf{m}_j^i)$ .

2. Perturb the measurements with inflated measurement noise:  $\mathbf{d}_{uc,j}^i \sim \mathcal{N}(\mathbf{d}, \alpha_i \mathbf{C}_D)$ .
3. Compute the cross covariance matrix  $\mathbf{C}_{MD}^i$  and the auto-covariance matrix of the predicted data  $\mathbf{C}_{DD}^i$ .
4. Update the ensemble as in (12), but with  $\mathbf{C}_D$  replaced by  $\alpha_i \mathbf{C}_D$ :

$$\mathbf{m}_j^{i+1} = \mathbf{m}_j^i + \mathbf{C}_{MD}^i (\mathbf{C}_{DD}^i + \alpha_i \mathbf{C}_D)^{-1} [\mathbf{d}_{uc,j}^i - g(\mathbf{m}_j^i)], \quad j = 1, \dots, N_e. \quad (13)$$

The inverse,  $\mathbf{C}_i^{-1}$ , of the matrix  $\mathbf{C}_i = \mathbf{C}_{DD}^i + \alpha_i \mathbf{C}_D$  is approximated by its pseudo-inverse using a truncated singular value decomposition (TSVD).

### 3.2 CAAE Parameterization of Conductivity Field

Let the matrix  $\mathbf{k} \in \mathbb{R}^{W \times H \times D}$  denote the log-conductivity field  $\ln K(\mathbf{x})$  defined on a three-dimensional numerical grid, which consists of  $W$ ,  $H$  and  $D$  elements in the three spatial directions. We use CAAE to parameterize the high-dimensional  $\mathbf{k}$  with a low-dimensional latent variable  $\mathbf{z}$ . The CAAE consists of two components, a GAN and an autoencoder (AE).

The GAN (I. J. Goodfellow et al., 2014) is a DNN strategy for generating data from complex distributions without having to actually acquire the full PDF. This strategy comprises two networks: a generator  $\mathcal{G}(\cdot)$  that generates samples similar to  $\mathbf{k}$ ; and a discriminator  $\mathcal{D}(\cdot)$  that is trained to distinguish between the generated samples and the real data samples. By “playing an adversarial game”, the discriminator  $\mathcal{D}(\cdot)$  improves its ability to catch flaws in the generated samples, and the generator  $\mathcal{G}(\cdot)$  improves its capacity to generate realistic samples that try to trick the discriminator.

The AE learns a low-dimensional representation  $\mathbf{z}$  of the data  $\mathbf{k}$ , and then generates a reconstruction  $\hat{\mathbf{k}}$  from  $\mathbf{z}$  that closely matches the original data  $\mathbf{k}$ . The encoded latent variable  $\mathbf{z}$  is constructed to follow a PDF  $\pi(\mathbf{z})$  that is easy to sample from, e.g., a standard normal PDF  $\mathcal{N}(\mathbf{0}, \mathbf{I})$ . A variational autoencoder (VAE) (Kingma & Welling, 2013) forces the empirical PDF of  $\mathbf{z}$  computed from the samples of  $\mathbf{k}$ ,  $\pi(\mathbf{z}|\mathbf{k})$ , to be close to the target PDF  $\pi(\mathbf{z})$  by adding the Kullback-Leibler divergence  $\text{KL}[\pi(\mathbf{z}|\mathbf{k})||\pi(\mathbf{z})]$  between the empirical and target PDFs to the total loss function:

$$\mathcal{L}_{\text{VAE}} = \mathcal{L}_{\text{rec}}(\mathbf{k}, \hat{\mathbf{k}}) + \text{KL}[\pi(\mathbf{z}|\mathbf{k})||\pi(\mathbf{z})], \quad (14)$$

where  $\mathcal{L}_{\text{rec}}(\mathbf{k}, \hat{\mathbf{k}})$  is the discrepancy between the data  $\mathbf{k}$  and their reconstruction  $\hat{\mathbf{k}}$ . Choices of this discrepancy function include  $L_1$  or  $L_2$  norm. We use the former to define the average reconstruction error  $\mathcal{L}_{\text{rec}}$  over  $N$  training samples,

$$\mathcal{L}_{\text{rec}} = \frac{1}{N} \sum_{i=1}^N \|\mathbf{k}_i - \hat{\mathbf{k}}_i\|_1. \quad (15)$$

The CAAE differs from the VAE in the way it minimizes the discrepancy between the empirical PDF  $\pi(\mathbf{z}|\mathbf{k})$  and the target PDF  $\pi(\mathbf{z})$  of the latent random variable  $\mathbf{z}$ . Instead of minimizing the KL divergence  $\text{KL}[\pi(\mathbf{z}|\mathbf{k})||\pi(\mathbf{z})]$ , the adversarial autoencoder (AAE) employs an adversarial training procedure to minimize this discrepancy. The training of the encoder  $\mathcal{G}(\cdot)$ , decoder  $\text{De}(\cdot)$ , and the discriminator  $\mathcal{D}(\cdot)$  is divided into the reconstruction phase and the regularization phase (Makhzani et al., 2016). Parameters in the encoder and decoder are updated by minimizing the loss function:

$$\mathcal{L}_{\text{ED}} = \mathcal{L}_{\text{rec}} + w\mathcal{L}_{\mathcal{G}}. \quad (16)$$

We use  $\mathcal{L}_{\mathcal{G}}$  to quantify the decoder’s ability to trick the discriminator,

$$\mathcal{L}_{\mathcal{G}} = -\frac{1}{N} \sum_{i=1}^N \ln \{ \mathcal{D}[\mathcal{G}(\mathbf{k}_i)] \}. \quad (17)$$

The weight factor  $w$  in (16) is used to assign relative importance to these two sources of error. In the simulations reported below, we set  $w = 0.01$ .

After the encoder and decoder are updated in the first training phase, the discriminator  $\mathcal{D}(\cdot)$  is trained in the second phase to minimize the loss function:

$$\mathcal{L}_{\mathcal{D}} = -\frac{1}{N} \sum_{i=1}^N \left\{ \ln [\mathcal{D}(\mathbf{z}_i)] + \ln [1 - \mathcal{D}(\mathcal{G}(\mathbf{k}_i))] \right\}. \quad (18)$$

By iterating between these two training phases, one obtains the mappings from  $\mathbf{k}$  to  $\mathbf{z}$  and from  $\mathbf{z}$  to  $\hat{\mathbf{k}}$ , and the decoder reaches its goal of constructing realizations  $\hat{\mathbf{k}}_i$  similar to the data  $\mathbf{k}_i$ .

The architectures of each network in the CAAE in this study are adopted from (Mo et al., 2019b), and illustrated with our modified schematics in Appendix A. We applied slight modifications to fit the dimensions and specifics of the problem in this study.

### 3.3 DenseED Neural Networks as Forward Model Surrogates

ESMDA inversion requires a large number of forward solves of the PDE-based model (1)–(8) for multiple realizations of the parameters  $\mathbf{m}$ . To alleviate the cost of each forward run, we replace the PDE-based model with a CNN surrogate.

Several approaches to constructing an input-output surrogate are collated in Table 2. We choose an autoregressive image-to-image (i-to-i) regression model, rather than its image-to-sparse-observation counterpart, because of its superior generalizability (Z. Zhou & Tartakovsky, 2021). We choose an autoregressive i-to-i model over a one-to-many i-to-i model based on computer-memory considerations: for three-dimensional problems with  $I$  time steps, memory allocated for input and output can be prohibitively large; also, the autoregressive scheme reduces the number of DNN parameters needed for the regression task. The source location ( $\mathbf{S}_{l,t}$ ) and strength ( $\mathbf{S}_{s,t}$ ) for the release period  $[t, t + \Delta t]$  are assembled into a three-dimensional matrix  $\mathbf{S}(\mathbf{x}, t) \in \mathbb{R}^{W \times H \times D}$ .

**Table 2.** Alternative input-output frameworks for construction of a surrogate model. The data are collected at  $M$  locations  $\mathbf{x}_m$  ( $m = 1, \dots, M$ ) at  $I$  times  $t_i$  ( $i = 1, \dots, I$ ). The source location ( $\mathbf{S}_{l,t}$ ) and strength ( $\mathbf{S}_{s,t}$ ) for the release period  $[t, t + \Delta t]$  are assembled into a three-dimensional matrix  $\mathbf{S}(\mathbf{x}, t)$ .

Model	Input	Output	Modeling frequency
PDE model	$\mathbf{m}$	$c(\mathbf{x}, t_i), h(\mathbf{x})$	1
Image-to-image	$\mathbf{m}$	$c(\mathbf{x}, t_i), h(\mathbf{x})$	1
Image-to-sensors	$\mathbf{m}$	$c(\mathbf{x}_m, t_i), h(\mathbf{x}_m)$	1
Autoregressive i-to-i	$c(\mathbf{x}, t), \ln K(\mathbf{x}), S(\mathbf{x}, t)$	$c(\mathbf{x}, t + \Delta t), h(\mathbf{x})$	$I$

An autoregressive surrogate  $\mathbf{NN}_{\text{auto}}$  replaces the PDF-based model:

$$\mathbf{g} : \mathbf{m} \xrightarrow{\text{PDEs}} \{c(x_m, t_i), h(x_m)\}_{m,i=1}^{M,I} \quad (19)$$

with a CNN that sequentially ( $I$  times) predicts the system state at the next time step,

$$\mathbf{NN}_{\text{auto}} : c(\mathbf{x}, t_i), K(\mathbf{x}), S(\mathbf{x}, t_i) \xrightarrow{\text{CNN}} \{c(\mathbf{x}, t_{i+1}), h(\mathbf{x})\}, \quad i = 0, \dots, I - 1. \quad (20)$$

If the three-dimensional simulation domain is discretized with a  $D \times H \times W$  grid, then the autoregressive CNN surrogate  $\mathbf{NN}_{\text{auto}}$  performs the following input-to-output mapping:

$$\mathbf{NN}_{\text{auto}} : \mathbb{R}^{n_x \times W \times H \times D} \rightarrow \mathbb{R}^{n_y \times W \times H \times D}, \quad (21)$$

where  $n_x = 3$ , denotes the three channels representing the concentration  $c(\mathbf{x}, t_i)$  and source terms  $S(\mathbf{x}, t_i)$  at time  $t_i$ , and the log-conductivity  $\ln K(\mathbf{x})$ ; and  $n_y = 2$  designates the two output channels representing the concentration  $c(\mathbf{x}, t_{i+1})$  at time  $t_{i+1}$  and the hydraulic head  $h(\mathbf{x})$ . A representative input-to-output example is shown in Figure 1.

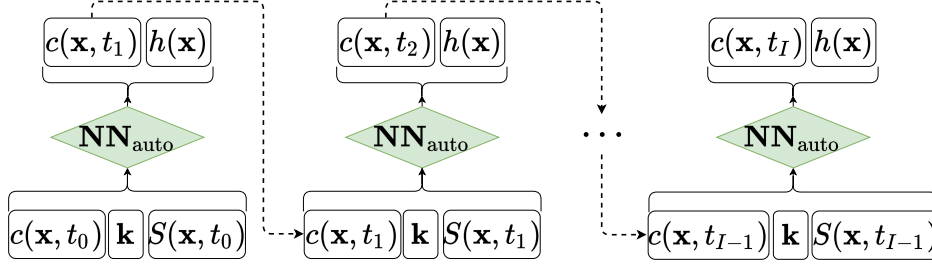


**Figure 1.** Autoregressive surrogate  $\mathbf{NN}_{\text{auto}}$  of the PDE-based flow and transport model (1)–(8). The three input channels correspond to  $c(\mathbf{x}, t)$ ,  $S(\mathbf{x}, t)$ , and  $\ln K(\mathbf{x})$ . The two output channels correspond to  $c(\mathbf{x}, t + \Delta t)$  and  $h(\mathbf{x})$ . The concentration values at all time steps  $t_{i=1}^I$  are obtained through the iteration prediction with the autoregressive model.

We use a three-dimensional DenseED architecture to solve the image-to-image regression task with a coarsen-refine process, with the convolutional operations. The encoder extracts the high-level coarse features of the input maps, while the decoder subsequently refines the coarse features to the full maps (Mo et al., 2019a, Fig. 2). We use the  $L_1$ -norm loss function, the  $L_2$ -norm weight regularization, and stochastic gradient descent (Bottou, 2010) in the CNN training process. A detailed description of this surrogate model and its training procedure can be found in Appendix A, and (Mo et al., 2019a). We have extended their procedure by adding the measurement locations to the loss function. This allows us to penalize the prediction error at these specific locations.

### 3.4 CAAE–DenseED–ESMDA Inversion Framework

We combine the CAAE parameterization of the conductivity field with the DenseED CNN surrogate of the forward model to obtain fast and accurate predictions of concentration  $c(\mathbf{x}, t)$  and  $h(\mathbf{x})$  for a given set of inputs. Then, we utilize ESMDA to identify the unknown parameters, including the conductivity field and the source terms ( $\mathbf{S}_i$ ,  $\mathbf{S}_s$ ). The CAAE parameterization enables one to estimate the discretized log-conductivity field  $\mathbf{k}$  through the latent variable  $\mathbf{z}$ . Our CAAE–DenseED–ESMDA inversion framework is implemented in the following algorithm.

1. Train a CAAE; obtain the decoder  $\text{De}(\cdot)$  that maps the low-dimensional latent variable  $\mathbf{z}$  back onto the log-conductivity field  $\mathbf{k}$ .
2. Train an autoregressive DenseED CNN  $\mathbf{NN}_{\text{auto}}$  to predict  $c(\mathbf{x}, t)$  and  $h(\mathbf{x})$  for a given conductivity field and contaminant release history.
3. Generate the initial input ensemble  $\mathbf{M}^f$  of size  $N_e$ , whose elements  $\mathbf{m}_j^1$  ( $j = 1, \dots, N_e$ ) are defined as  $\mathbf{m}_j^1 = (\mathbf{z}_j^1, \mathbf{S}_{i,j}^1, \mathbf{S}_{s,j}^1)^\top$ . Here,  $\mathbf{z}_j^1 \sim \mathcal{N}(\mathbf{0}, \mathbf{I}_z)$  is the latent

- variable for the log conductivity field; and  $\mathbf{S}_{1j}^1$  and  $\mathbf{S}_{sj}^1$  denote respectively the source location and strength in all release periods, drawn from an appropriate prior distribution.
4. Perform the ESM DA inversion with  $N_a$  data assimilation iterations and the inflation coefficients  $\alpha_i$  ( $i = 1, \dots, N_a$ ). For  $i = 1, \dots, N_a$ ,
    - (a) Obtain the log-conductivity realizations  $\mathbf{k}_j^i = \text{De}(\mathbf{z}_j^i)$  with  $j = 1, \dots, N_e$ ;
    - (b) Form the release configuration  $\{\mathbf{S}_{1,j}^i, \mathbf{S}_{s,j}^i\}$  into the input matrix  $\mathbf{S}_j^i$ , and predict  $c(\mathbf{x}, t)$  and  $h(\mathbf{x})$  at the measurement times and locations,  $\text{NN}_{\text{auto}}(\mathbf{m}_j^i)$  for all  $j$ ;
    - (c) Update the ensemble  $\mathbf{m}_j^i$  via ESM DA with  $\alpha_i$  to obtain  $\mathbf{m}_j^{i+1}$ .
  5. The end result,  $\mathbf{m}_j^{N_a+1}$ , serves as the final ensemble from which PDFs of the log conductivity field and the contaminant release parameters are estimated.

This algorithm is illustrated in the schematic in Figure 2 as well.

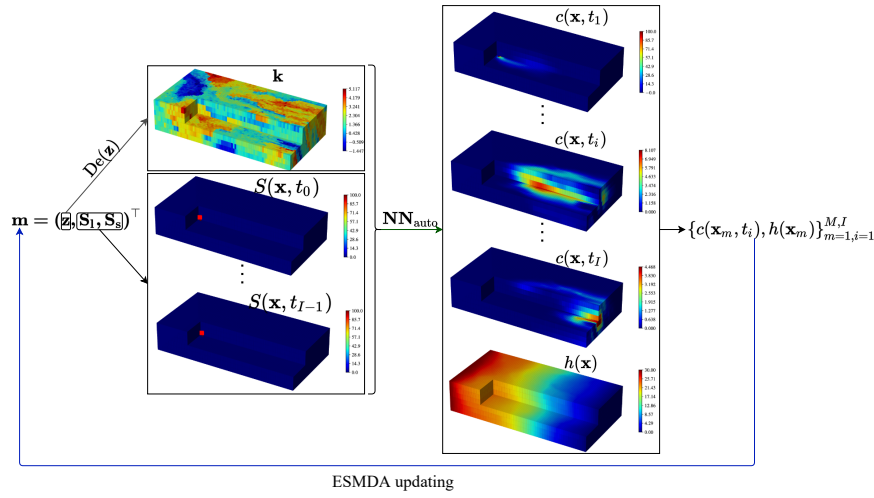


**Figure 2.** Schematic illustrating the CAAE-DenseED-ESMDA algorithm.  $\text{De}(\cdot)$  denotes the decoder that obtains the log-conductivity field from the latent variable  $\mathbf{z}$ ,  $\text{NN}_{\text{auto}}$  represents the autoregressive surrogate model which predicts the concentration and hydraulic head fields. The observations at the measurement time and locations  $c(\mathbf{x}_m, t_i), h(\mathbf{x}_m)$  are then used to update the parameter  $\mathbf{m}$ .

## 4 Numerical experiments

### 4.1 Experimental Setup

A confined heterogeneous aquifer is described as a rectangular cuboid  $\Omega$  of size  $2500 \text{ m} \times 1250 \text{ m} \times 300 \text{ m}$ ; it is discretized with a mesh consisting of  $81 \times 41 \times 6$  cells. Groundwater flow is driven by constant heads  $h_L = 30 \text{ m}$  and  $h_R = 0 \text{ m}$  imposed along the left ( $x_1 = 0$ ) and right ( $x_1 = 2500 \text{ m}$ ) facets of the cuboid, respectively; the remaining boundaries are impermeable to flow. The hydraulic conductivity of this aquifer,  $K(\mathbf{x})$ , is unknown (except when generating the ground truth); equiprobable realizations of  $Y(\mathbf{x}) = \ln K(\mathbf{x})$  are generated by extracting  $81 \times 41 \times 6$  patches from the  $150 \text{ px} \times 180 \text{ px} \times 120 \text{ px}$  training image (Mariethoz & Kelly, 2011) in Figure 3, available at <https://github.com/GAIA-UNIL/trainingimages>. One such cropped



log-conductivity field  $Y(\mathbf{x})$  and the corresponding hydraulic head  $h(\mathbf{x})$ , obtained as a solution of the groundwater flow equation (1), are shown in Figure 4. These fields serve as the ground truth.

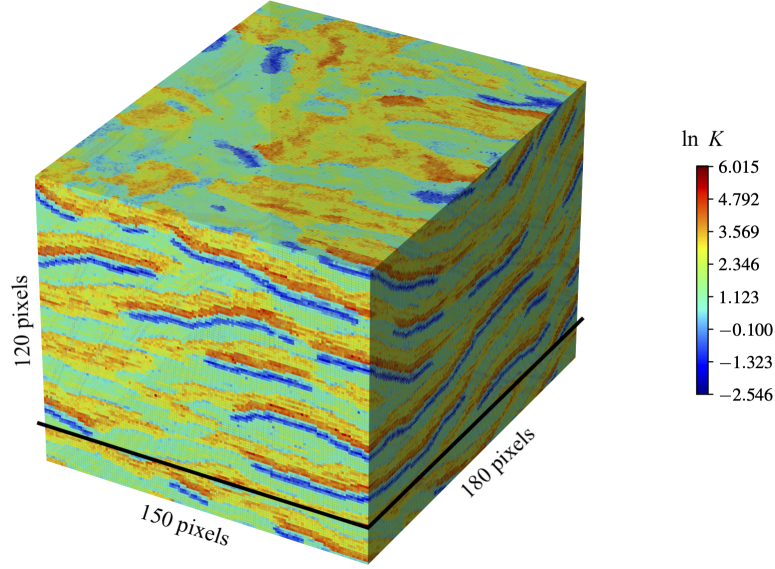


**Figure 3.** Training image, consisting of  $150 \times 180 \times 120$  pixels. Equiprobable realizations of log-conductivity  $Y(\mathbf{x}) = \ln K(\mathbf{x})$  are generated by randomly selecting patches of size  $81 \times 41 \times 6$  pixels. The top  $150 \times 180 \times 105$  pixels serve as the training set. The bottom  $150 \times 180 \times 15$  pixels serve as the testing set. Conductivity  $K$  is in m/d.

The porosity  $\theta$  and bulk density  $\rho$  of the soil; dispersivities  $\alpha_L$ ,  $\alpha_T$  and  $\alpha_C$ ; and the parameters  $K_f$  and  $a$  of the Freundlich isotherm are constant. Values of these transport parameters, which are representative of a sandy alluvial aquifer in Southern California (Liggett et al., 2015), are presented in Table 3. The contaminant enters the aquifer via a point source, whose depth is known (the fourth layer from the top of the domain) but the location in the horizontal plane ( $S_1^x$  and  $S_1^y$ ) is uncertain. The contaminant release is known to occur during a 20-year period, but its strength is uncertain. Following the standard practice in groundwater modeling, we divide this time interval into  $N_{re} = 5$  sub-intervals (“stress periods” in the MODFLOW/MT3D language) during each of which the release strength ( $S_s$ ) is constant. In this configuration, the unknown contaminant release history is represented by the vector  $\mathbf{S} = (\mathbf{S}_1, \mathbf{S}_s)$ , where  $\mathbf{S}_1 = (S_1^x, S_1^y)^\top$  and  $\mathbf{S}_s = (S_{s,1}, S_{s,2}, S_{s,3}, S_{s,4}, S_{s,5})^\top$ . The values of  $\mathbf{S}$  used to generate the ground-truth concentrations are reported in Table 4. Combined with the discretized version  $\mathbf{k}$  of the uncertain log-conductivity field  $Y(\mathbf{x})$ , this yields 19933 unknowns to be determined from the measurements of solute concentration  $c(\mathbf{x}, t)$  and hydraulic head  $h(\mathbf{x})$ . Expert knowledge about possible location and strength of the contaminant release is encapsulated in the uniform (“uninformative”) prior distributions for  $\mathbf{S}_1$  and  $\mathbf{S}_s$ , which are shown in Table 4.

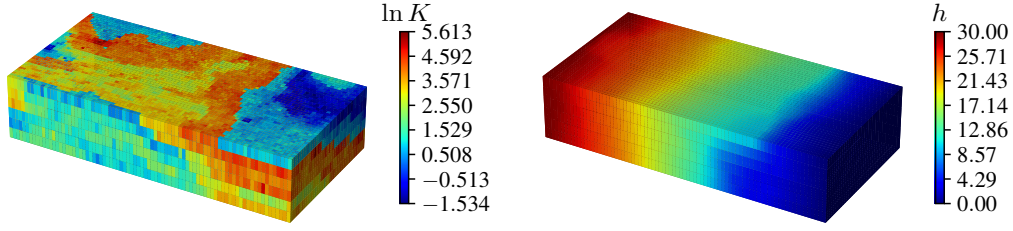


**Figure 4.** Log-conductivity  $Y(\mathbf{x})$  (left) and the corresponding hydraulic head  $h(\mathbf{x})$  (right), which serve as ground truth and to generate measurements of  $h$  at observation wells. Conductivity  $K$  is in m/d and head  $h$  in m.

**Table 3.** Values of the transport parameters for a dissolved contaminant migrating in a generic sandy alluvial aquifer in Southern California (Liggett et al., 2015).

Property	Value	Units
$\phi$	0.3	—
$K_f$	0.1	(m <sup>3</sup> /g) <sup>a</sup>
$a$	0.9	—
$\rho$	1587	kg/m <sup>3</sup>
$\alpha_L$	35	m
$\alpha_T/\alpha_L$	0.3	—
$\alpha_C/\alpha_L$	0.3	—
$D_m$	10 <sup>-9</sup>	m <sup>2</sup> /d

**Table 4.** Parameters  $\mathbf{S}_l = (S_l^x, S_l^y)^\top$  and  $\mathbf{S}_s = (S_{s,1}, S_{s,2}, S_{s,3}, S_{s,4}, S_{s,5})^\top$  used to represent, respectively, the location and strength of a contaminant release. Reported as “Truth” are their (unknown) reference values used to generate ground truth and concentration measurements, and “Prior” the intervals on which their uniform priors,  $\mathcal{U}[\cdot, \cdot]$ , are defined. The values of  $\mathbf{S}_l$  are in m, and of  $\mathbf{S}_s$  in g/m<sup>3</sup>.

	$S_l^x$	$S_l^y$	$S_{s,1}$	$S_{s,2}$	$S_{s,3}$	$S_{s,4}$	$S_{s,5}$
Truth	291	625	224	174	869	201	741
Prior	[125, 625]	[125, 1125]	[50, 1000]	[50, 1000]	[50, 1000]	[50, 1000]	[50, 1000]

These measurements are collected at observations wells, whose completion allows one to collect water samples in each of the model’s six vertical layers. We consider the observation wells whose locations are depicted in Figure 5. During the simulated time horizon of 40 years, the contaminant concentration is sampled at  $I = 10$  time intervals of four years each, and the hydraulic head is measured once since the flow is at steady-state. The data at all space-time locations are generated by adding zero-mean Gaussian measurement error with standard deviations  $\sigma_c = \sigma_h = 0.5$ , to the solution  $\mathbf{g}(\mathbf{m})$  of the flow and transport model (1)–(8) with the input parameter values identified as “ground truth” above, corresponding to 2.5% of the maximum value of the concentration ( $\sim 20 \text{ g/m}^3$ ), and  $\sim 1.7\%$  of the maximum value of the hydraulic head ( $\sim 30 \text{ m}$ ) on all sensor locations.

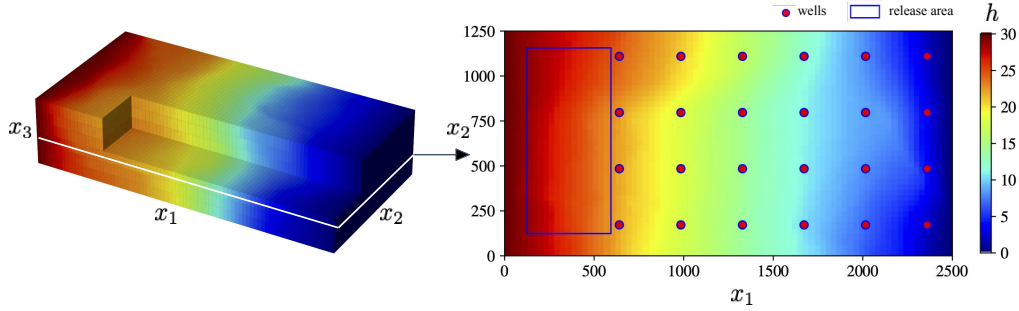


**Figure 5.** Observational wells (red dots) in which measurements of hydraulic head  $h$  and solute concentration  $c$  are collected. The well locations are superposed on the ground-truth distribution of hydraulic head in the fourth layer of the MODFLOW model. The blue box represents a region of possible contaminant release from a point source that is known to be located in the fourth model-layer,  $x_1, x_2, x_3$  in m.

## 4.2 CAAE Training for Conductivity Parameterization

We train a CAAE DNN to parameterize the discretized log-conductivity field  $\mathbf{k} \in \mathbb{R}^{81 \times 41 \times 6}$ . The end goal is an encoder  $\mathcal{G}(\mathbf{k})$  that maps an input field  $\mathbf{k}$  onto a low-dimensional latent variable  $\mathbf{z} \in \mathbb{R}^{2 \times 2 \times 11 \times 21}$  with standard-Gaussian prior  $\mathcal{N}(\mathbf{0}, \mathbf{I})$ , and a decoder  $\text{De}(\cdot)$  that reconstructs  $\mathbf{k}$  from this latent variable. The training is done on 23000 realizations of  $\mathbf{k}$ , obtained as randomly selected  $(81 \times 41 \times 6)$  patches from the top  $150 \text{ px} \times 180 \text{ px} \times 105 \text{ px}$  part of the large training image in Figure 3. Additional 2200 images cropped from the bottom  $150 \text{ px} \times 180 \text{ px} \times 15 \text{ px}$  part of the training image serve as the testing set. The latent variable  $\mathbf{z}$  has  $2 \cdot 2 \cdot 11 \cdot 21 = 924$  elements. With 50-epochs training and the learning rate of  $2 \cdot 10^{-4}$ , the Adam optimizer is used to obtain the DNN parameters and, thus, build  $\mathcal{G}(\mathbf{k})$  and  $\text{De}(\mathbf{z})$ . The details of the CAAE architecture are explained in Appendix A, and the dimensions of the internal layers outputs are listed in Table 6.

A representative realization of  $\ln K(\mathbf{x}) \mapsto \mathbf{k}$  from the test set and its reconstruction via the decoder,  $\hat{\mathbf{k}} = \text{De}(\mathbf{z})$ , are shown in Figure 6. After the training is complete, the mean absolute error  $\|\mathbf{k} - \hat{\mathbf{k}}\|_1$ , averaged over all the elements of the numerical mesh and over the 2200 members of the testing data set, is 0.2637. The reconstructed log-conductivity field  $\hat{\mathbf{k}}$  captures the main structural features of its original counterpart  $\mathbf{k}$ . Some loss of information is unavoidable in reduced-order modeling but, overall, the performance of this autoencoder is adequate to achieve accurate inverse modeling results, as we show in Section 4.4 below.

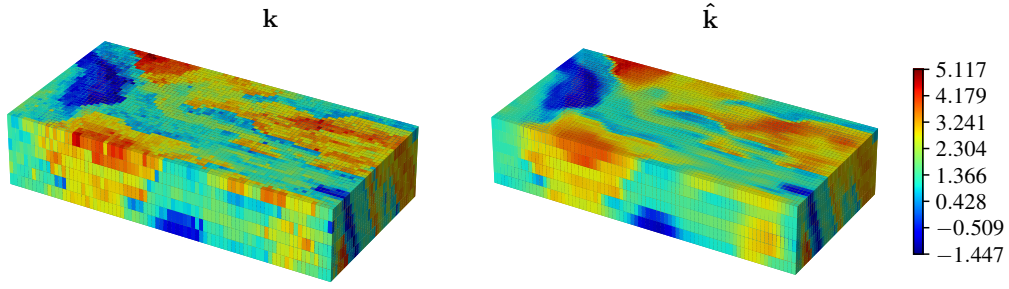


**Figure 6.** A representative realization of  $\ln K(\mathbf{x}) \mapsto \mathbf{k}$  from the test set (left) and its reconstruction (right) via the CAAE encoder,  $\mathbf{z} = \mathcal{G}(\mathbf{k})$ , and decoder,  $\hat{\mathbf{k}} = \mathcal{D}(\mathbf{z})$ .

### 4.3 DenseED Surrogate Model

As mentioned in Section 3, although only model predictions at the well locations are necessary for the inversion, a DNN that predicts  $c(\mathbf{x}, t_i)$  and  $h(\mathbf{x})$  at all points  $\mathbf{x}$  of the simulation domain has better generalization properties. We train our CNN on  $N = 800$  Monte Carlo realizations of the PDE-based model (1)–(8) with corresponding realizations of the input parameters  $\mathbf{m}$  (the discretized log-conductivity  $\mathbf{k}$  and contaminant release history  $\mathbf{S}$ ). Another set of  $N_{\text{test}} = 150$  realizations are retained for testing. These 950 realizations form  $950 \times 10$  autoregressive input-output pairs. The CNN contains three dense blocks with  $N_l = 3, 6$ , and 3 internal layers, has the growth rate of  $R_g = 48$  and  $N_{\text{in}} = 48$  initial features; it was trained for 200 epochs with the learning rate of  $5 \cdot 10^{-3}$ . We use the  $L_1$ -norm loss function and the  $L_2$ -norm weight regularization, apply stochastic gradient descent (Bottou, 2010) in the parameter estimation process, and add 5 times the  $L_1$ -norm loss at the source pixel and its surrounding pixels, 5 times the  $L_1$ -norm loss at the well locations to the total loss to penalize the prediction error at the source locations and the observation wells. The CNN’s output is the hydraulic head  $h(\mathbf{x})$  and the solute concentration  $c(\mathbf{x}, t_i)$  at the next time step  $t_i$ . The details of the architecture are explained in Appendix A and the dimensions of the internal layers outputs are listed in Table 7.

Figure 7 exhibits temporal snapshots of the solute concentrations alternatively predicted with the PDE-based model solved with MODFLOW and MT3DMS simulators,  $c(\mathbf{x}, t_i)$ , and the CNN surrogate,  $\hat{c}(\mathbf{x}, t_i)$ , for a given realization of the log-conductivity field and the contaminant release configuration (both drawn from the test set). Also presented are the hydraulic head maps predicted by the autoregressive model,  $\hat{h}(\mathbf{x})$ , and the PDE-based model solved with MODFLOW simulator,  $h(\mathbf{x})$ . The accuracy of our CNN surrogate is quantified by the total root mean square error,  $(\|c(\mathbf{x}, t) - \hat{c}(\mathbf{x}, t)\|_2 + \|h(\mathbf{x}) - \hat{h}(\mathbf{x})\|_2)/2$ . It falls to 0.853 at the end of the training process. It is worthwhile emphasizing here that the  $N_{\text{NMC}} = 800$  Monte Carlo realizations used to train the CNN surrogate are but a small fraction of the forward runs required by ESMDA inversion framework. One could achieve more accurate predictions for three-dimensional problems by either deploying a more complex DNN architecture (Wen et al., 2021; Mo et al., 2019b) or using much larger  $N_{\text{NMC}}$  or both. However, similar to the CAAE training, we focus on the development of efficient methodologies for three-

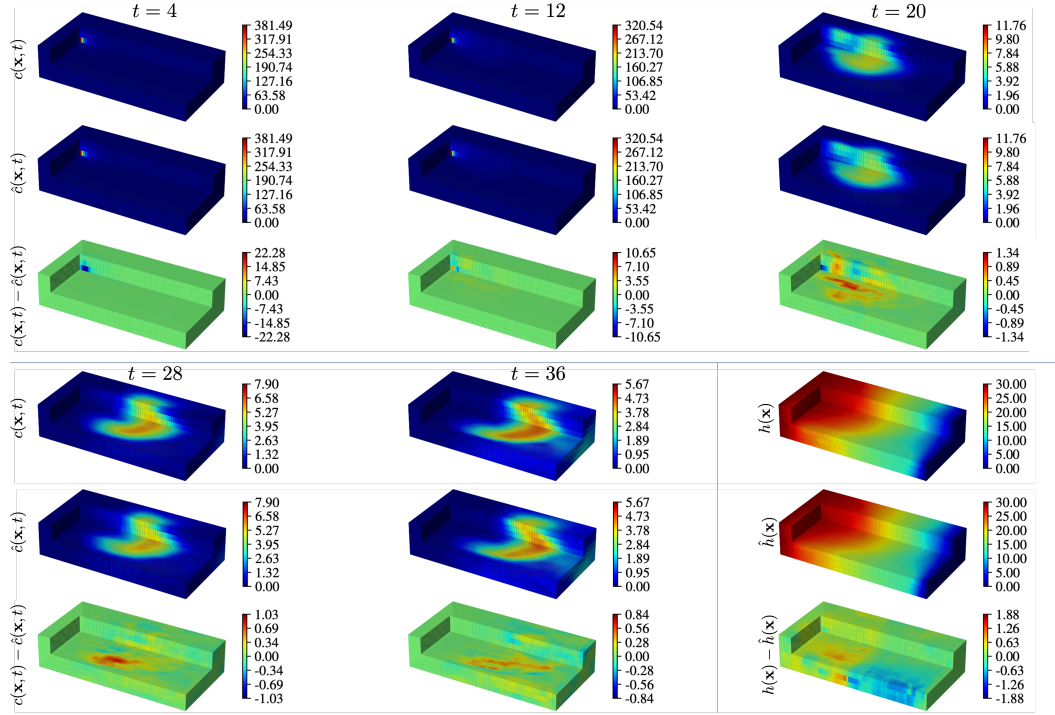


**Figure 7.** Predictions of the solute concentration obtained with the PDE-based model,  $c(\mathbf{x}, t)$ , and its DenseED CNN surrogate,  $\hat{c}(\mathbf{x}, t)$ , times  $t = 4, 12, 20, 28, 36$ ,  $t$  in year. Also shown are the corresponding predictions of the hydraulic head,  $h(\mathbf{x})$  and  $\hat{h}(\mathbf{x})$ ; and the difference between these two types  $c(\mathbf{x}, t) - \hat{c}(\mathbf{x}, t)$ ,  $h(\mathbf{x}) - \hat{h}(\mathbf{x})$  of prediction.

dimensional inverse modeling that accommodate the trade-off between the accuracy and computational feasibility.

#### 4.4 ESMDA Inversion

We demonstrate the use of the CAAE parameterization and the DenseED CNN surrogate of the PDE-based forward model to accelerate the ESMDA inversion. The combination of these three techniques constitutes our CAAE-DenseED-ESMDA framework to approximate the joint posterior PDF of the uncertain model parameters  $\mathbf{m}$  consistent with both model predictions and field observations. In the simulations reported below, we select  $N_a = 10$  inflation factors in (13) and set their values to  $\alpha_i = 10$  for  $i = 1, \dots, N_a$ , and perform ESMDA with 10 iterations. To ascertain the impact of the DenseED CNN surrogate on the inversion accuracy, we also run CAAE-ESMDA with the PDE-based forward model implemented in MODFLOW and MT3DMS. The ensemble size for ESMDA for both CAAE-ESMDA and CAAE-DenseED-ESMDA are set to  $N_e = 960$ .

The measurements are taken at 24 wells that are completed in all 6 layers of the model, yielding  $24 \cdot 6 = 144$  measurements of the solute concentration and hydraulic head at each observation time, the hydraulic head is only measured once, resulting in  $144 \cdot (10 + 1) = 1584$  measurements in 40 years of the modeling time.

Figure 8 exhibits posterior statistics (mean  $\langle Y \rangle$  and standard deviation  $\sigma_Y$ ) of the log-conductivity  $Y(\mathbf{x})$ , obtained after the assimilation of all 1584 measurements via either CAAE-ESMDA or CAAE-DenseED-ESMDA. In both scenarios, the posterior ensemble mean  $\langle Y \rangle$ , reconstructed from the latent variable  $\mathbf{z}$ , correctly identifies the low-conductivity region in the right top region of the three-dimensional domain and the high-conductivity regions elsewhere. As expected, the mean log-conductivity fields,  $\langle Y \rangle$ , are smoother than the reference field  $Y$  (Figure 4), but the realizations drawn from the posterior Gaussian PDF  $\mathcal{N}(\langle Y \rangle, \sigma_Y)$  exhibit more realistic features (right column in Figure 8). Regardless of the forward model used (the only difference in these two experiments), our data assimilation framework yields consistent predictions of  $\sigma_Y$  (middle column in Figure 8). It is small throughout most of the domain, indicating the reduced uncertainty in the estimation of hydraulic conductivity  $K(\mathbf{x})$  due to assimilation of the concentration and head measurements. The maximum values of  $\sigma_Y$  and, hence, the largest predictive uncertainty in the  $K(\mathbf{x})$  estimation, are along the interface between the high- and low-conductivity regions. This finding suggests that the model predictions of hydraulic head and solute concentration are least sensitive to the changes in hydraulic conductivity in that domain; it reaffirms the conclusion of the sensitivity analysis of the relative importance of uncertainties in the spatial arrangement of hydrofacies and their hydraulic conductivities (Winter et al., 2006).

The same inversion experiments yield estimates of the contaminant release history  $\mathbf{S}$ , which are shown in Figures 9 and Figure 10 for CAAE-ESMDA and CAAE-DenseED-ESMDA, respectively. Regardless of the forward model used, our inversion algorithm accurately estimates the release strength during stress periods 1, 2, and 3 ( $S_{s,1}$ ,  $S_{s,2}$ , and  $S_{s,3}$ ); the estimates are close to their reference values and have tight 95% confidence intervals. At the same time, the estimates of the source strength during stress periods 4 and 5 ( $S_{s,4}$  and  $S_{s,5}$ ) fail to converge to their reference values and exhibit large error bars. The two assimilation strategies yield very similar estimates of the contaminant release location,  $\mathbf{S}_1 = (S_1^x, S_1^y)^\top$ ; the estimates of both quantities have tight confidence intervals, but the estimated value of  $S_1^x$  for CAAE-DenseED-ESMDA inversion lies slightly farther from the reference value than that of CAAE-ESMDA.



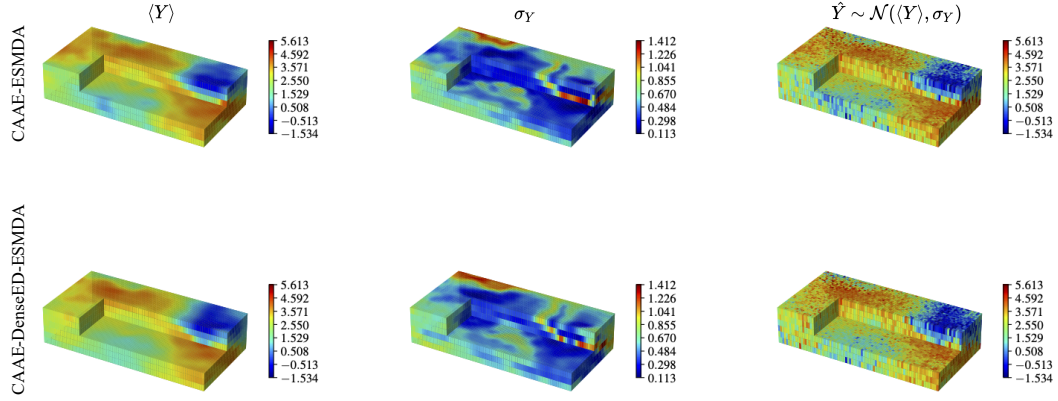


**Figure 8.** Posterior mean ( $\langle Y \rangle$ , left column) and standard deviation ( $\sigma_Y$ , middle column) of the log-conductivity field  $Y(\mathbf{x})$  obtained upon assimilation of concentration and head measurements from the dense observation network. These statistics are obtained via our inversion algorithm CAAE-ESMDA that relies on either the PDE-based forward model (top row) or its DenseED CNN surrogate (CAAE-DenseED-ESMDA, bottom row). Also shown are representative realizations of  $Y(\mathbf{x})$  drawn from the resulting posterior PDF  $\mathcal{N}(\langle Y \rangle, \sigma_Y)$  (right column).

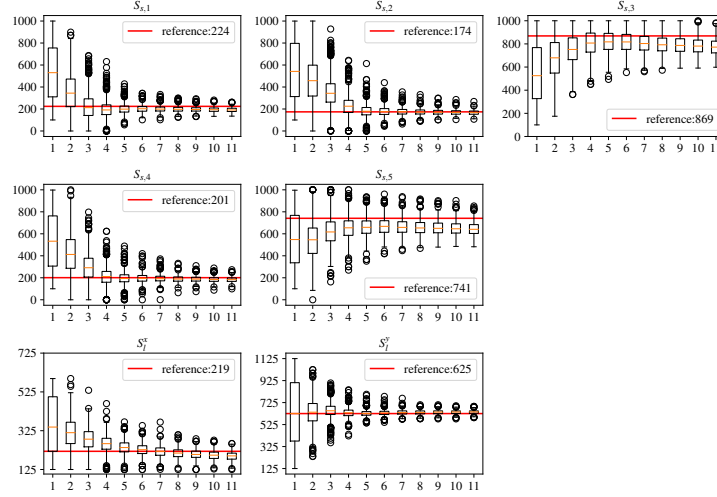


**Figure 9.** Boxplots of the ensembles for the contaminant release terms,  $\mathbf{S} = (\mathbf{S}_l, \mathbf{S}_s)$  with  $\mathbf{S}_l = (S_l^x, S_l^y)^\top$  and  $\mathbf{S}_s = (S_{s,1}, \dots, S_{s,5})^\top$ , and their confidence intervals, obtained via the CAAE-ESMDA inversion with the PDE-based forward model. These quantities are plotted as function of the ESMDA iterations and contrasted with their reference values (horizontal lines). The source location  $\mathbf{S}_l$  is in  $m$ ; and the contaminant release strength in each of the five stress periods,  $\mathbf{S}_s$ , is in  $g/m^3$ .



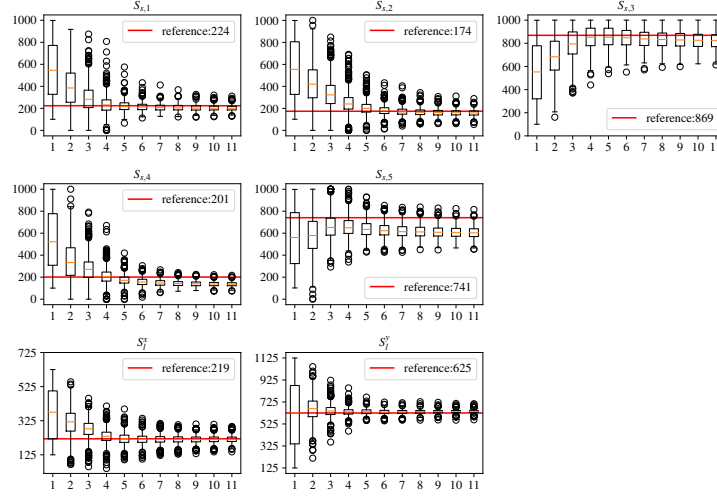


**Figure 10.** Boxplots of the ensembles for the contaminant release terms,  $\mathbf{S} = (\mathbf{S}_l, \mathbf{S}_s)$  with  $\mathbf{S}_l = (S_l^x, S_l^y)^\top$  and  $\mathbf{S}_s = (S_{s,1}, \dots, S_{s,5})^\top$ , and their confidence intervals, obtained via the CAAE-ESMDA inversion with the DenseED CNN surrogate. These quantities are plotted as function of the ESMDA iterations and contrasted with their reference values (horizontal lines). The source location  $\mathbf{S}_l$  is in  $m$ ; and the contaminant release strength in each of the five stress periods,  $\mathbf{S}_s$ , is in  $g/m^3$ .

#### 4.5 Comparison of Computational Costs

The computational costs of CAAE-ESMDA with the PDE-based forward model and its counterpart with the DenseED CNN surrogate are shown in Table 5. CAAE-ESMDA with the PDE-based model ran on CPU, while the DenseED CNN surrogate was trained and simulated on GPUs provided by GoogleColab. In both cases, ESMDA consists of  $N_e = 960$  samples in each ensemble and 10 iterations are performed, resulting in  $N_{\text{sum}} = N_e \times (10 + 1) = 10560$  forward model runs. Overall, CAAE-DenseED-ESMDA is two-orders of magnitude faster than CAAE-ESMDA with the PDE-based forward model.

**Table 5.** Total run time of the CAAE-ESMDA,  $T_{\text{run}}$ , includes the costs of the PDE-based forward model and its CNN surrogate. The average run-time per sample,  $T_{\text{ave}}$ , is defined as  $T_{\text{ave}} = (T_{\text{run}} + T_{\text{dataset}} + T_{\text{train}})/N_{\text{sum}}$ , where  $T_{\text{dataset}}$  is the time for obtaining the training and testing data sets, and  $T_{\text{train}}$  is the CNN training time. CAAE parameterization is used in both cases, the training time is 18678.23, the running time of CAAE is negligible in both data assimilation strategies. All times are in seconds.

	$T_{\text{run}}$	$T_{\text{dataset}}$	$T_{\text{train}}$	$T_{\text{ave}}$
CAAE-ESMDA	360885.0	0.0	0.0	36.8
CAAE-DenseED-ESMDA	1893.9	34922.0	9439.2	4.4

## 5 Conclusions and Discussion

We proposed an CAAE-DenseED-ESMDA algorithm to infer the statistics of both aquifer properties (e.g., hydraulic conductivity) and contaminant release history from sparse and noisy observations of hydraulic head and solute concentration. The algorithm relies on CAEE to obtain a low-dimensional representation of the high-dimensional discretized conductivity field (and, if necessary, other spatially distributed input parameters); deploys a DenseED CNN surrogate of the PDE-based transport model to accelerate the forward runs; and adopts ESMDA to solve the inverse problem. The algorithm’s computational efficiency is such that it enables one to handle three-dimensional problems.

To demonstrate the salient features of our inversion methodology, we conduct a series of numerical experiments. They deal with flow and transport in a three-dimensional heterogeneous aquifer with uncertain hydraulic conductivity field; our goal is to estimate the latter, and the contaminant release history, from the measurements of hydraulic head and contaminant concentration collected in a few observation wells. These numerical experiments lead to the following conclusions.

1. The CAAE-DenseED-ESMDA inversion framework is capable of both identifying the contaminant release source and reconstructing a three-dimensional hydraulic conductivity field from sparse (in space and time) and noisy measurements of solute concentration and hydraulic head.
2. The CAAE-ESMDA inversion, with or without the DenseED CNN surrogate of the PDE-based forward model, yields estimates of the contaminant release strength that differ from the reference values by up to 30.42%. That can be attributed to the imperfect reconstruction of hydraulic conductivity field or relative insensitivity of the observed solute concentrations to the contaminant release strengths in each stress period (the inverse problem’s ill-posedness).
3. Deployment of the DenseED CNN surrogate within our CAAE-ESMDA inversion framework provides an order of magnitude speed up, while giving identical estimates of the hydraulic conductivity field; it also increases the predictive uncertainty (posterior standard deviation) relative to that obtained via the CAAE-ESMDA inversion with the PDE-based model.
4. The computational efficiency of CAAE-DenseED-ESMDA, relative to that of CAAE-ESMDA with the high-fidelity PDE model, is mostly due to the use of GPUs for CNN-related computations, while the PDE solver for the flow and transport model (e.g., MODFLOW and MT3DMS) utilizes CPUs.
5. Deployment of CAAE-DenseED-ESMDA allows one to investigate questions, such as measuring the data assimilation accuracy versus the ensemble size or designing a network of observation wells, that cannot be answered with CAAE-ESMDA with the PDE-based forward model, whose computational cost might be prohibitive.

Although the flow and transport simulators, MODFLOW and MT3DMS, can be parallelized to run on multiple CPU cores, that is a much more arduous task than carrying out NN-related computations on GPUs available in Google-Colab or other cloud computing environments. The latter takes very little implementation effort and can be done on a personal computer. The advantage of our method largely depends on the feasibility of accessing GPU computing resources versus deploying multicores parallelization with the physics-based forward model.

## Acknowledgements

NZ acknowledges support from ARPA-E (award # DE-AR0001204).

## Appendix A

The following sections discuss the details of the DNNs used in this study: CAAE for the parameterization of the hydraulic conductivity field, and the DenseED surrogate model predicting the groundwater flow and the contaminant transport.

### CAAE

As briefly introduced in Section 3.2, the CAAE consists of three networks: an encoder ( $\mathcal{G}$ ), a decoder (De), and a discriminator ( $\mathcal{D}$ ). The workflow of these three networks and the architecture of each network are shown in Figure 11. The residual-in-residual dense block (RRDB) used in the encoder and the decoder is illustrated in Figure 12, in which the dense block is reused in the DenseED surrogate model as well, and is shown in Figure 14. The dimensions of the internal layers of the encoder and the decoder are shown in Table 6. Batch normalization (BN) (Ioffe & Szegedy, 2015), three dimensional convolutional operations (Conv) (I. Goodfellow et al., 2016), Sigmoid, ReLU and LeakyReLU nonlinear activation functions (He et al., 2015) are used in these neural networks; “FC(128)” denotes a fully-connected layer with the output vector length being 128, “Upsample” layer doubles the size of the input feature maps with the nearest upsampling method.

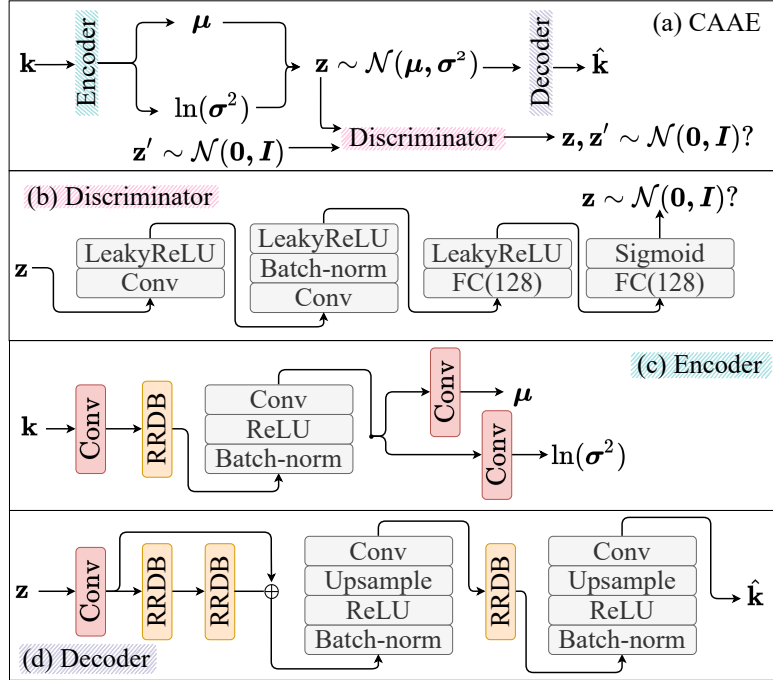


**Figure 11.** (a) CAAE, (b) Discriminator, (c) Encoder, and (d) Decoder. The CAAE (a) consists of an encoder (c) and a decoder (d), the discriminator (b) is trained as well to enforce the distribution of the low-dimensional latent variable  $\mathbf{z}$ . “RRDB” blocks are depicted in Figure 12, with the slope parameter in “LeakyReLU” being 0.2 in this study.  $\oplus$  denotes element-wise summation.

### DenseED

The architecture of the DenseED in this study is shown in Figure 13. The DenseED neural network structure consists of three main sub-structures: dense blocks,

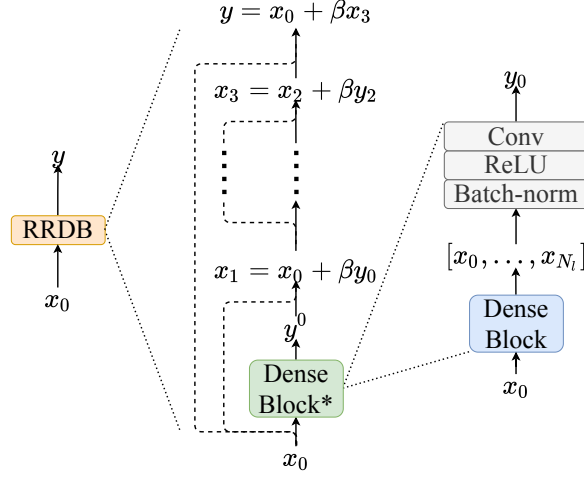


**Figure 12.** *RRDB block structure. Each RRDB block used in this study consists of  $N_{DB} = 3$  dense blocks, with the internal layer number of each dense block being  $N_l = 5$ . The dense block is illustrated in (a) in Figure 14.*

**Table 6.** *Dimension of the internal layer outputs of the encoder and decoder in CAAE. The encoder outputs  $\mu$  and  $\ln \sigma^2$ .  $N_{DB}$  denotes the number of dense blocks in a residual-in-residual block, shown in Figure 12.*

Encoder		
Layers	Number of features $C_f$	Resolution $W \times H \times D$
Input: $\mathbf{k}$	1	$81 \times 41 \times 6$
Conv	48	$41 \times 21 \times 3$
RRDB, $N_{DB} = 3$	48	$41 \times 21 \times 3$
BN-ReLU-Conv	48	$41 \times 21 \times 3$
Conv: $\mu$	2	$21 \times 11 \times 2$
Conv: $\ln \sigma^2$	2	$21 \times 11 \times 2$
Decoder		
Layers	Number of features $C_f$	Resolution $W \times H \times D$
Input: $\mathbf{z}$	2	$21 \times 11 \times 2$
Conv	48	$21 \times 11 \times 2$
RRDB, $N_{DB} = 3$	48	$21 \times 11 \times 2$
RRDB, $N_{DB} = 3$	48	$21 \times 11 \times 2$
BN-ReLU-UP-Conv	48	$41 \times 21 \times 4$
RRDB, $N_{DB} = 3$	48	$41 \times 21 \times 4$
BN-ReLU-UP-Conv: $\hat{\mathbf{k}}$	1	$81 \times 41 \times 6$

557 encoding layers, and decoding layers. The structure of a dense block is illustrated in  
 558 (a) in Figure 14. An encoding layer is shown in (b) in Figure 14, with which both  
 559 the feature number and the size of the features are halved:  $x^0 \in \mathbb{R}^{C \times W \times H \times D}$ ,  $x' \in$   
 560  $\mathbb{R}^{\frac{1}{2}C \times W \times H \times D}$ ,  $x^1 \in \mathbb{R}^{\frac{1}{2}C \times \frac{1}{2}W \times \frac{1}{2}H \times \frac{1}{2}D}$ . This figure can represent a decoding layer  
 561 as well, with the feature number halved, the size doubled:  $x^0 \in \mathbb{R}^{C \times W \times H \times D}$ ,  $x' \in$   
 562  $\mathbb{R}^{\frac{1}{2}C \times W \times H \times D}$ ,  $x^1 \in \mathbb{R}^{\frac{1}{2}C \times 2W \times 2H \times 2D}$ . In addition to these three main elements, the  
 563 size of the features are first halved with the very first Conv layer. The last decoding  
 564 layer maps the feature number to that of the output. The dimensions of the outputs  
 565 from each block are shown in Table 7.

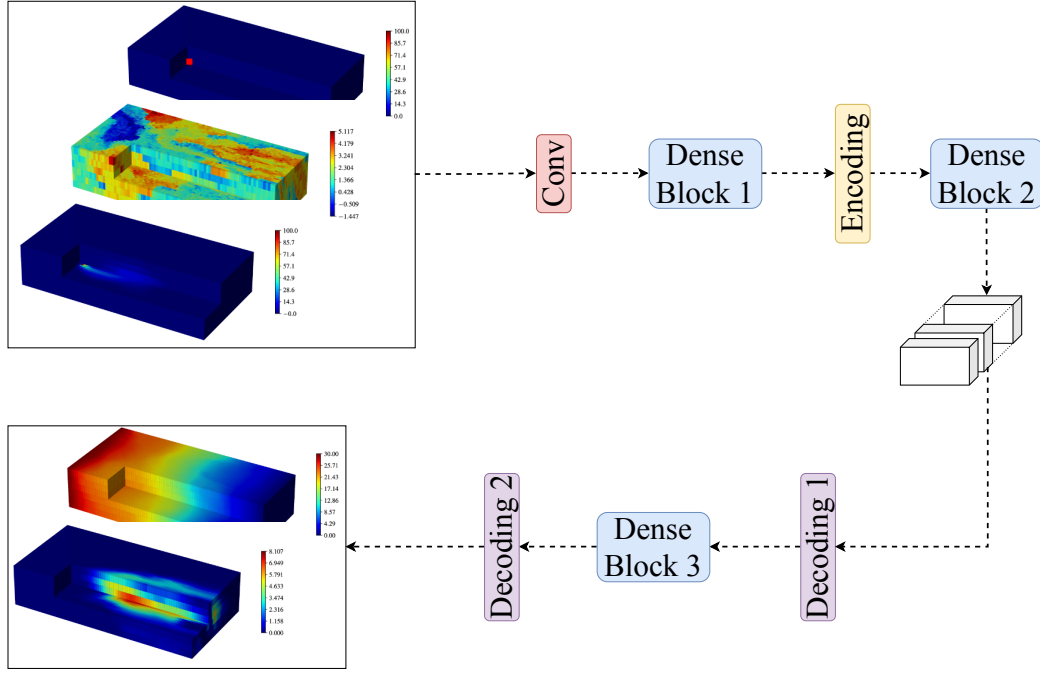


**Figure 13.** Dense encoder decoder (DenseED) architecture with three dense blocks. The cubes as the output of “Dense Block 2” represent the encoded coarse high-level features.

**Table 7.** Dimension of the internal layer outputs of the DenseED network.  $N_l$  is the number of the internal layers in a dense block shown in Figure 14.

Layer	Number of features $C_f$	Resolution $W \times H \times D$
Input: $(c(\mathbf{x}, t), \mathbf{k}, S(\mathbf{x}, t))$	3	$81 \times 41 \times 6$
Conv	48	$41 \times 21 \times 3$
Dense Block 1, $N_l = 3$	192	$41 \times 21 \times 3$
Encoding	96	$21 \times 11 \times 2$
Dense Block 2, $N_l = 6$	384	$21 \times 11 \times 2$
Decoding 1	192	$41 \times 21 \times 3$
Dense Block 3, $N_l = 3$	336	$41 \times 21 \times 3$
Decoding 2: $(c(\mathbf{x}, t + \Delta t), h(\mathbf{x}))$	2	$81 \times 41 \times 6$

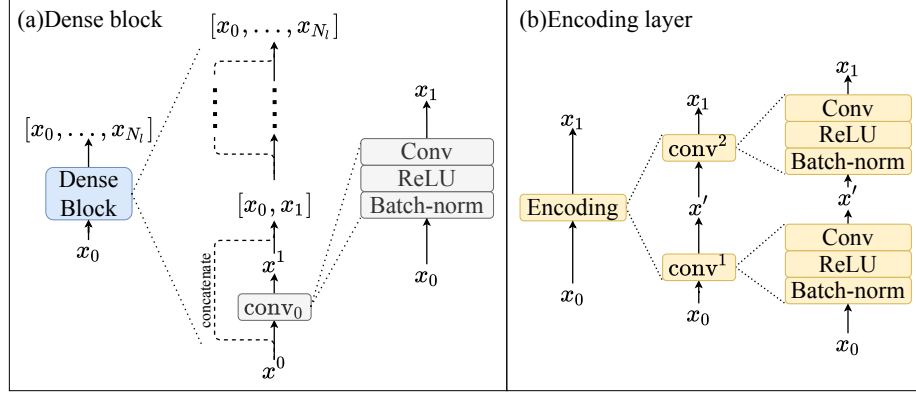


**Figure 14.** (a) A dense block with  $N_l$  internal layers. (b) Encoding layer structure in Figure 13. The feature number of  $x^0$  is halved first, then the size of the features are halved:  $x^0 \in \mathbb{R}^{C \times W \times H \times D}$ ,  $x' \in \mathbb{R}^{\frac{1}{2}C \times W \times H \times D}$ ,  $x^1 \in \mathbb{R}^{\frac{1}{2}C \times \frac{1}{2}W \times \frac{1}{2}H \times \frac{1}{2}D}$ .

## References

- Aral, M. M., Guan, J., & Maslia, M. L. (2001). Identification of contaminant source location and release history in aquifers. *Journal of hydrologic engineering*, 6(3), 225–234.
- Ayvaz, M. T. (2016). A hybrid simulation–optimization approach for solving the areal groundwater pollution source identification problems. *J. Hydrol.*, 538, 161–176.
- Bakker, M., Post, V., Langevin, C. D., Hughes, J. D., White, J., Starn, J., & Fienen, M. N. (2016). Scripting modflow model development using python and flopy. *Groundwater*, 54(5), 733–739.
- Barajas-Solano, D. A., Alexander, F. J., Anghel, M., & Tartakovsky, D. M. (2019). Efficient gHMC reconstruction of contaminant release history. *Front. Environ. Sci.*, 7, 149. doi: 10.3389/fenvs.2019.00149
- Bedekar, V., Morway, E. D., Langevin, C. D., & Tonkin, M. J. (2016). *MT3D-USGS version 1: A US Geological Survey release of MT3DMS updated with new and expanded transport capabilities for use with MODFLOW* (Tech. Rep.). Reston, VA: US Geological Survey.
- Boso, F., & Tartakovsky, D. M. (2020a). Data-informed method of distributions for hyperbolic conservation laws. *SIAM Journal on Scientific Computing*, 42(1), A559–A583.
- Boso, F., & Tartakovsky, D. M. (2020b). Learning on dynamic statistical manifolds. *Proceedings of the Royal Society A*, 476(2239), 20200213.
- Bottou, L. (2010). Large-scale machine learning with stochastic gradient descent. In *Proceedings of compstat'2010* (pp. 177–186). Springer.
- Canchumuni, S. W., Emerick, A. A., & Pacheco, M. A. C. (2019). History matching geological facies models based on ensemble smoother and deep generative models. *Journal of Petroleum Science and Engineering*, 177, 941–958.
- Chaudhuri, A., Hendricks-Franssen, H.-J., & Sekhar, M. (2018). Iterative filter based estimation of fully 3D heterogeneous fields of permeability and Mualem-van Genuchten parameters. *Adv. Water Resour.*, 122, 340–354.
- Emerick, A. A., & Reynolds, A. C. (2013). Ensemble smoother with multiple data assimilation. *Computers & Geosciences*, 55, 3–15. doi: https://doi.org/10.1016/j.cageo.2012.03.011
- Evensen, G. (1994). Sequential data assimilation with a nonlinear quasi-geostrophic model using monte carlo methods to forecast error statistics. *Journal of Geo-*

- physical Research: Oceans, 99(C5), 10143–10162.
- Evensen, G. (2003). The ensemble kalman filter: Theoretical formulation and practical implementation. *Ocean dynamics*, 53(4), 343–367.
- Gamerman, D., & Lopes, H. F. (2006). *Markov chain monte carlo: stochastic simulation for bayesian inference*. Chapman and Hall/CRC.
- Gao, G., & Reynolds, A. C. (2004). An improved implementation of the LBFGS algorithm for automatic history matching. In *Spe annual technical conference and exhibition*. doi: 10.2118/90058-MS
- Goodfellow, I., Bengio, Y., & Courville, A. (2016). *Deep learning*. MIT press.
- Goodfellow, I. J., Pouget-Abadie, J., Mirza, M., Xu, B., Warde-Farley, D., Ozair, S., ... Bengio, Y. (2014). Generative adversarial networks. *arXiv preprint arXiv:1406.2661*.
- Haario, H., Laine, M., Mira, A., & Saksman, E. (2006). DRAM: efficient adaptive MCMC. *Stat. Comput.*, 16(4), 339–354.
- Haario, H., Saksman, E., & Tamminen, J. (2001). An adaptive Metropolis algorithm. *Bernoulli*, 7(2), 223–242.
- Harbaugh, A. W. (2005). *MODFLOW-2005, the US Geological Survey modular ground-water model: the ground-water flow process*. Reston, VA: US Department of the Interior, US Geological Survey.
- He, K., Zhang, X., Ren, S., & Sun, J. (2015). Delving deep into rectifiers: Surpassing human-level performance on imagenet classification. In *Proceedings of the IEEE international conference on computer vision* (pp. 1026–1034).
- Ioffe, S., & Szegedy, C. (2015). Batch normalization: Accelerating deep network training by reducing internal covariate shift. In *International conference on machine learning* (pp. 448–456).
- Jiang, S., & Durlofsky, L. J. (2021). Data-space inversion using a recurrent autoencoder for time-series parameterization. *Computational Geosciences*, 25(1), 411–432.
- Ju, L., Zhang, J., Meng, L., Wu, L., & Zeng, L. (2018). An adaptive gaussian process-based iterative ensemble smoother for data assimilation. *Advances in water resources*, 115, 125–135.
- Kang, X., Kokkinaki, A., Kitanidis, P. K., Shi, X., Lee, J., Mo, S., & Wu, J. (2021). Hydrogeophysical characterization of nonstationary dnapi source zones by integrating a convolutional variational autoencoder and ensemble smoother. *Water Resources Research*, 57(2), e2020WR028538.
- Kang, X., Kokkinaki, A., Kitanidis, P. K., Shi, X., Revil, A., Lee, J., ... Wu, J. (2020). Improved characterization of dnapi source zones via sequential hydrogeophysical inversion of hydraulic-head, self-potential and partitioning tracer data. *Water Resources Research*, 56(8), e2020WR027627.
- Kim, S., Min, B., Kwon, S., & Chu, M.-g. (2019). History matching of a channelized reservoir using a serial denoising autoencoder integrated with es-mds. *Geofluids*, 2019.
- Kingma, D. P., & Welling, M. (2013). Auto-encoding variational bayes. *arXiv preprint arXiv:1312.6114*.
- Leichombam, S., & Bhattacharjya, R. K. (2018). New hybrid optimization methodology to identify pollution sources considering the source locations and source flux as unknown. *J. Hazar. Tox. Radioact. Waste*, 23(1), 04018037.
- Liggett, J. E., Partington, D., Frei, S., Werner, A. D., Simmons, C. T., & Fleckenstein, J. H. (2015). An exploration of coupled surface–subsurface solute transport in a fully integrated catchment model. *Journal of Hydrology*, 529, 969–979.
- Linde, N., Renard, P., Mukerji, T., & Caers, J. (2015). Geological realism in hydrogeological and geophysical inverse modeling: A review. *Advances in Water Resources*, 86, 86–101.
- Liu, Y., Sun, W., & Durlofsky, L. J. (2019). A deep-learning-based geological param-



- eterization for history matching complex models. *Mathematical Geosciences*, 51(6), 725–766.
- Makhzani, A., Shlens, J., Jaitly, N., & Goodfellow, I. (2016). Adversarial autoencoders. In *International Conference on Learning Representations (ICLR)*.
- Mariethoz, G., & Kelly, B. F. (2011). Modeling complex geological structures with elementary training images and transform-invariant distances. *Water Resources Research*, 47(7).
- Mo, S., Zabaras, N., Shi, X., & Wu, J. (2019a). Deep autoregressive neural networks for high-dimensional inverse problems in groundwater contaminant source identification. *Water Resources Research*, 55(5), 3856–3881.
- Mo, S., Zabaras, N., Shi, X., & Wu, J. (2019b). Integration of adversarial autoencoders with residual dense convolutional networks for inversion of solute transport in non-gaussian conductivity fields. *arXiv preprint arXiv:1906.11828*.
- Sarma, P., Durlofsky, L. J., & Aziz, K. (2008). Kernel principal component analysis for efficient, differentiable parameterization of multipoint geostatistics. *Mathematical Geosciences*, 40(1), 3–32.
- Snodgrass, M. F., & Kitanidis, P. K. (1997). A geostatistical approach to contaminant source identification. *Water Resources Research*, 33(4), 537–546.
- Tang, M., Liu, Y., & Durlofsky, L. J. (2021). Deep-learning-based surrogate flow modeling and geological parameterization for data assimilation in 3d subsurface flow. *Computer Methods in Applied Mechanics and Engineering*, 376, 113636.
- Tartakovsky, D. M., & Winter, C. L. (2008). Uncertain future of hydrogeology. *Journal of Hydrologic Engineering*, 13(1), 37–39.
- Van Leeuwen, P. J., & Evensen, G. (1996). Data assimilation and inverse methods in terms of a probabilistic formulation. *Monthly Weather Review*, 124(12), 2898–2913.
- Vo, H. X., & Durlofsky, L. J. (2014). A new differentiable parameterization based on principal component analysis for the low-dimensional representation of complex geological models. *Mathematical Geosciences*, 46(7), 775–813.
- Wen, G., Tang, M., & Benson, S. M. (2021). Towards a predictor for co2 plume migration using deep neural networks. *International Journal of Greenhouse Gas Control*, 105, 103223.
- White, R. E. (2015). Nonlinear least squares algorithm for identification of hazards. *Cogent Math.*, 2(1), 1118219.
- Winter, C. L., Guadagnini, A., Nychka, D., & Tartakovsky, D. M. (2006). Multivariate sensitivity analysis of saturated flow through simulated highly heterogeneous groundwater aquifers. *J. Comput. Phys.*, 217(1), 166–175.
- Winter, C. L., Tartakovsky, D. M., & Guadagnini, A. (2003). Moment equations for flow in highly heterogeneous porous media. *Surveys in Geophysics*, 24(1), 81–106.
- Wu, Z., Reynolds, A. C., & Oliver, D. S. (1999). Conditioning geostatistical models to two-phase production data. *SPE journal*, 4(02), 142–155.
- Xia, Y., & Zabaras, N. (2021). Bayesian multiscale deep generative model for the solution of high-dimensional inverse problems. *arXiv preprint arXiv:2102.03169*.
- Xu, T., & Gómez-Hernández, J. J. (2016). Joint identification of contaminant source location, initial release time, and initial solute concentration in an aquifer via ensemble Kalman filtering. *Water Resour. Res.*, 52(8), 6587–6595.
- Xu, T., & Gómez-Hernández, J. J. (2018). Simultaneous identification of a contaminant source and hydraulic conductivity via the restart normal-score ensemble Kalman filter. *Adv. Water Resour.*, 112, 106–123.
- Yang, H.-J., Boso, F., Tchelepi, H. A., & Tartakovsky, D. M. (2020). Method of distributions for quantification of geologic uncertainty in flow simulations. *Water Resources Research*, 56(7), e2020WR027643. doi: 10.1029/2020WR027643
- Yeh, H.-D., Chang, T.-H., & Lin, Y.-C. (2007). Groundwater contaminant source

- 711 identification by a hybrid heuristic approach. *Water Resources Research*,  
712 43(9).
- 713 Zhang, J., Lin, G., Li, W., Wu, L., & Zeng, L. (2018). An iterative local updating  
714 ensemble smoother for estimation and uncertainty assessment of hydrologic  
715 model parameters with multimodal distributions. *Water Resources Research*,  
716 54(3), 1716–1733.
- 717 Zhang, J., Zeng, L., Chen, C., Chen, D., & Wu, L. (2015). Efficient bayesian experi-  
718 mental design for contaminant source identification. *Water Resources Research*,  
719 51(1), 576–598.
- 720 Zheng, C., & Wang, P. P. (1999). *MT3DMS: a modular three-dimensional multi-*  
721 *species transport model for simulation of advection, dispersion, and chemical*  
722 *reactions of contaminants in groundwater systems; documentation and user’s*  
723 *guide*. Environmental Laboratory (US).
- 724 Zhou, H., Gómez-Hernández, J. J., & Li, L. (2014). Inverse methods in hydrogeol-  
725 ogy: Evolution and recent trends. *Advances in Water Resources*, 63, 22–37.
- 726 Zhou, Z., & Tartakovsky, D. M. (2021). Markov chain monte carlo with neural net-  
727 work surrogates: Application to contaminant source identification. *Stochastic*  
728 *Environmental Research and Risk Assessment*, 35(3), 639–651.